Investigation of the multiaxial fatigue behaviour of 316 stainless steel based on critical plane method

A.S Cruces[1], P. Lopez-Crespo[1*], S. Bressan[2], T. Itoh[3]

[1]Department of Civil and Materials Engineering, University of Malaga, C/Dr Ortiz Ramos s/n, 29071, Malaga, Spain
[2]Graduate School of Science & Engineering, Ritsumeikan University,1-1-1, Nojihigashi, Kusatsu-shi, Shiga, 525-8577, Japan
[3]Department of Mechanical Engineering, College of Science & Engineering, Ritsumeikan University, 1-1-1, Nojihigashi, Kusatsu-shi, Shiga 525-8577, Japan

ABSTRACT.

In this work the multiaxial behaviour of 316 stainless steel is studied under the lens of critical plane approach. A series of experiments were developed on dog bone shaped hollow cylindrical specimens made of type 316 stainless steel. Five different loading conditions were assessed with: (i) only tensile axial stress, (ii) only hoop stress, (iii) combination of axial and hoop stresses with square shape, (iv) combination of tensile axial and hoop stresses with L-shape and (v) combination of compressive axial and hoop stresses with L-shape. The fatigue analysis is performed with four different critical plane theories, namely Wang-Brown, Fatemi-Socie, Liu I and Liu II. The efficiency of all four theories is studied in terms of the accuracy of their life predictions and crack failure plane angle. The best fatigue life predictions were obtained with Liu II model and the best predictions of the failure plane were obtained with Liu I model.

KEYWORDS

Multiaxial fatigue; Biaxial fatigue; Life evaluation; Non-proportional loading; Critical plane method; 316 stainless steel; Ratchetting;

---

[*] Corresponding author: plopezcrespo@uma.es

Nomenclature

b	Fatigue strength exponent
b_γ	Fatigue torsional strength exponent
c	Fatigue ductility exponent
c_γ	Fatigue torsional ductility exponent
E	Young Modulus
G	Shear modulus
k	Fatemi-Socie material parameter
N_{exp}	Experimental fatigue life
N_f	Fatigue life, number of cycles
N_{mod}	Fatigue life calculated by the model
n'_γ	Cyclic torsional hardening exponent
S	Wang-Brown material parameter
γ'_f	Fatigue torsional ductility coefficient
ΔW_I	Liu I cyclic work
ΔW_{II}	Liu II cyclic work
$\Delta\gamma$	Shear strain range
$\Delta\varepsilon$	Normal strain range
$\Delta\sigma$	Axial stress range
$\Delta\tau$	Shear stress range
ε_{eqa}	Von Mises equivalent strain amplitude
ε_{eqm}	Von Mises equivalent mean strain
ε'_f	Fatigue ductility coefficient
σ'_f	Fatigue strength coefficient
$\sigma_{n,max}$	Maximum axial stress at critical plane
$\sigma_{n,mean}$	Mean axial stress at critical plane
σ'_y	Cyclic yield strength
σ_{ys}	Yield strength
τ'_f	Fatigue strength coefficient
υ_e	Poisson’s ration in elastic deformation
υ_p	Poisson’s ration in plastic deformation
φ^*	Critical plane

1. INTRODUCTION

Fatigue characterisation of engineering materials usually starts by conducting uniaxial studies. The results of uniaxial tests can be used to make rough estimations of the fatigue behaviour under more complex multiaxial loading. Uniaxial fatigue methods, based on these experimental data can generate good results for proportional multiaxial loading in some cases, as it was observed by Paguga et al with different materials [1]. Nevertheless, better estimations under complex multiaxial loading scenarios can be achieved by conducting experimental tests with these complex scenarios. Such conditions are often more similar to the conditions that real components are subjected to [2]. Nevertheless, since multiaxial experiments are very difficult to conduct and very time consuming, the amount of data available in the literature under such complex loading scenarios is very scarce and not enough for developing robust models to improve current fatigue predictions [3]. The predictions given by classical methodology under complex loading conditions is not always conservative because some interaction effects are not considered [4,5]. The critical plane approach is a very useful tool for predicting not only the fatigue life, but also the cracking angle under multiaxial conditions by taking into account the stress state and some interaction effects that appear along the loading cycle. All this information are contained in a damage parameter [6]. Critical plane methods can be classified as (i) stress-based, (ii) strain-based and (iii) energy-based [6]. The quality of the predictions depends on the type and quality of the experimental information used for feeding the model and the loading conditions [7]. Sophisticated damage parameters which include several loading effects have been presented [6,8]. Good correlation between experimental and estimated fatigue lives has been observed for a number of cases. For example, the Liu II critical plane model has been able to predict satisfactorily the fatigue life of 316 stainless steel material under axial and torsion conditions [9]. In addition Fatemi-Socie model was able to give accurate predictions for St52-3N [10]. Nevertheless, in order to make achieve good predictions with critical plane models, a good key information about the multiaxial behaviour of the material is required.

The 316 stainless steel material is commonly used in industry for structural and piping applications [11–15], because of its good corrosion resistance and good mechanical properties at high temperature. The 316H creep-fatigue behaviour was investigated, with tubular specimens subjected to variable axial strain with different levels of inner pressure [16]. Results showed that holding both the tensile and the compressive loads has a higher detrimental effect on the fatigue life. Increasing the inner pressure reduces the fatigue life and also strain hardens the material. A similar study was developed using 316 stainless steel for different proportional and non-proportional loading paths under inner and outer pressure [17]. Results showed again the detrimental effect of increase the inner pressure for the fatigue life, but a negligible effect of the outer pressure. New creep models for 316L were developed and extended to creep-fatigue to estimate fatigue life, however very conservative results were returned [18]. The multiaxial behaviour of 316L stainless steel was also investigated with different critical plane models under strain control [19]. Both proportional and non-proportional loading conditions were studied with different combinations of tension, compression and torsion.

In this work the multiaxial 316 stainless steel fatigue behaviour is studied with several well-established critical plane methods [10,20–23]; Fatemi-Socie, Wang-Brown, Liu I and Liu II models,with an emphasis on a type of loading (inner pressure) that often appears in 316 piping and vessels applications. The present work is based on different loading paths aimed at evaluating the ability of different critical plane models to take into account effects such as hardening or mean stress for fatigue life prediction and crack plane angle. The critical planes that are used in this study take into account the mean stress effect and thus are most appropriate for ductile behaviour such as that of 316 stainless steel.

2. MATERIALS AND METHODS

The experiments were conducted on 316 stainless steel specimens subjected to a quenching heat treatment (1050 ºC, WQ). The chemical composition is summarised in Table 1.

Table 1. Chemical composition of 316 stainless steel (in wt.%)

C	Si	Mn	P	S	Ni	Cr	Mo
0.06	0.46	1.33	0.32	0.28	10.15	16.97	2.03

The experimental program was conducted on a three actuator testing machine, to control (i) axial force, (ii) reversed torsion and (iii) introduce pressure into the specimen. Fig. 1 shows the experimental setup with the directions adopted in this work. Hollow cylindrical dog bone shaped specimens were used based on ASTM axial-torsional fatigue tests[24]. The dimensions of the specimens are shown in Fig. 2. The average inner and gauge surface roughness is 1.6μm. The surface finish was improved by polishing the central gauge part of the specimen with 1 μm alumina particles. The inner surface of the specimen was also polished with SiC paper with grade up to #2000. The surface finish in the inner surface of the specimen was not as good as the outer surface due to the machining procedure. The inner surface was polished using SiC paper with axial movements in four stages, covering the entire inner surface.

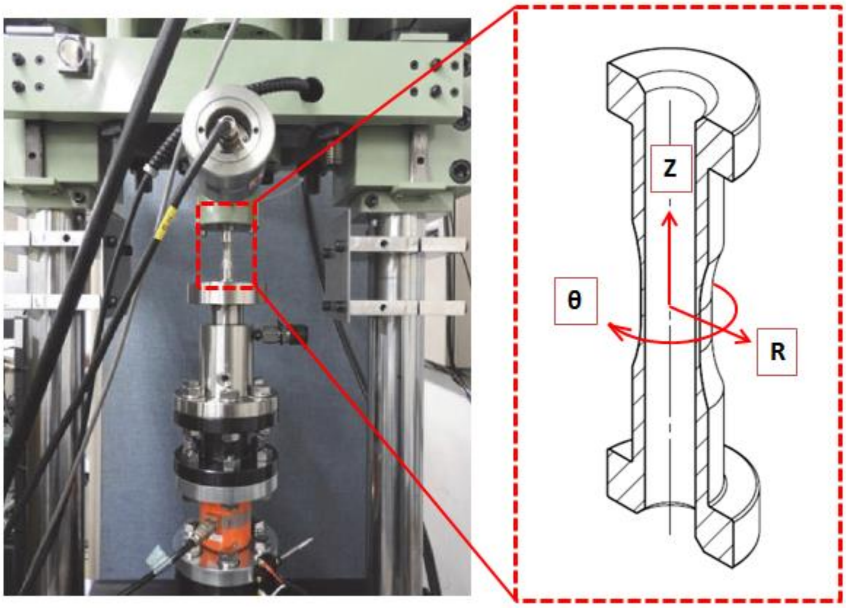

Figure 1. Experimental setup and directions adopted in this work.

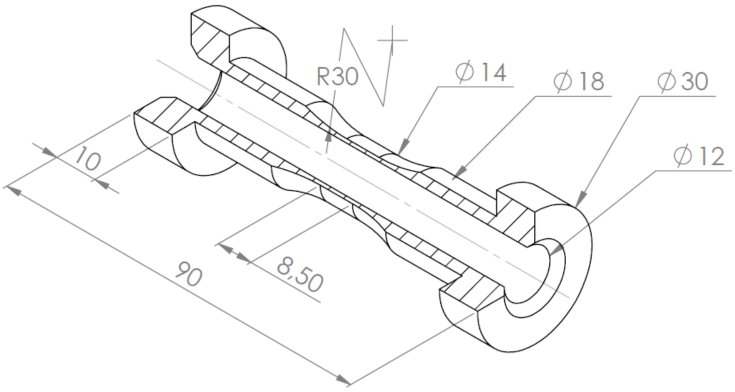

Figure 2. Geometry of the specimen. All dimensions are in mm.

The monotonic and cyclic properties are summarised in Tables 2 and 3, respectively. 316 stainless steel cyclic uniaxial properties are from foreign origin [11] Table 3. Specimens were subjected to eight different strain amplitudes under strain control with a frequency of 0.5 Hz. The cyclic torsional properties were obtained from cyclic uniaxial properties with von Mises equivalence [6] and are summarised in Table 4.

Table 2. Monotonic properties 316 stainless steel

Young modulus	Shear modulus	Elastic Poisson coefficient	Plastic Poisson coefficient	Yield Stress
193 GPa	75 GPa	0.3	0.5	240 MPa

Table 3. Cyclic uniaxial properties 316 stainless steel

Cyclic strength coefficient	Cyclic hardening coefficient	Fatigue strength coefficient	Fatigue strength exponent	Fatigue ductility coefficient	Fatigue ductility exponent
899 MPa	0.1901	663.25 MPa	-0.0903	0.1895	-0.4657

Table 4. Cyclic torsional properties 316 stainless steel

Fatigue torsional strength coefficient	Fatigue torsional strength exponent	Fatigue torsional ductility coefficient	Fatigue torsional ductility exponent
382.92 MPa	-0.0903	0.03282	-0.4657

3. MULTIAXIAL EXPERIMENTAL PROGRAM

Tests with different loading paths were carried out under force/pressure control while measuring the axial and the hoop strains on the outer surface. All experiments were conducted at room temperature. Table 5 shows the loading paths applied, the test identification ID, the axial stress amplitude σ_{Za}, the hoop stress amplitude $\sigma_{\theta a}$, the radial stress amplitude σ_{Ra}, the amplitude and mean strain for axial and hoop direction at half-life fatigue on the outer surface (except the radial stress amplitude) ε_{za}, ε_{zm}, $\varepsilon_{\theta a}$ and $\varepsilon_{\theta m}$ and total fatigue life N_f for each test. The loading paths 1 and 6 were repeated with two different loads and are referred to with letter A and B in Table 5. All the loading paths studied were proportional because of the principal directions being constant [6]. The fatigue failure in all the tests was detected by a pressure drop. In order to also detect the failure in samples 1 and 3, a small inner pressure was also applied in these tests (5th column in Table 5). Each loading path has been performed only once because of the complexity and long time required for this type of test [17,25,26]. However it can be observed that appear a relation between each loading path and the fatigue life obtained [27]. Fig. 3 shows a schematic of the six loading paths studied.

Table 5. Test details of the six different loading paths studied.

Loading path	ID	σ_{Za} (MPa)	$\sigma_{\theta a}$ (MPa)	σ_{Ra} (MPa)	ε_{za} (%)	ε_{zm} (%)	$\varepsilon_{\theta a}$ (%)	$\varepsilon_{\theta m}$ (%)	N_f (cycles)
Pull	1A	256.05	0.88	0.5	0.34	9.38	0.10	-6.5	122000
Pull	1B	227.57	1.024	0.46	0.17	7.62	0.03	-1.6	159600
Inner-pressure	2	16.723	224.81	32.67	0.11	-0.8	0.27	5.1	29300
Push-pull	3	442.9	0.969	0.47	0.8	13.3	0.193	-2.56	785
Square-shape	4	188.08	206.6	30.7	0.22	6.713	0.18	4.33	8400
LT-shape	5	174.65	173.87	28.4	0.20	0.4	0.29	0.34	14486
LC-shape	6A	201.54	225.2	32.77	0.1	-3	0.24	5.31	25770
LC-shape	6B	222.75	255.2	36.22	0.12	-5.7	0.24	6.2	13542

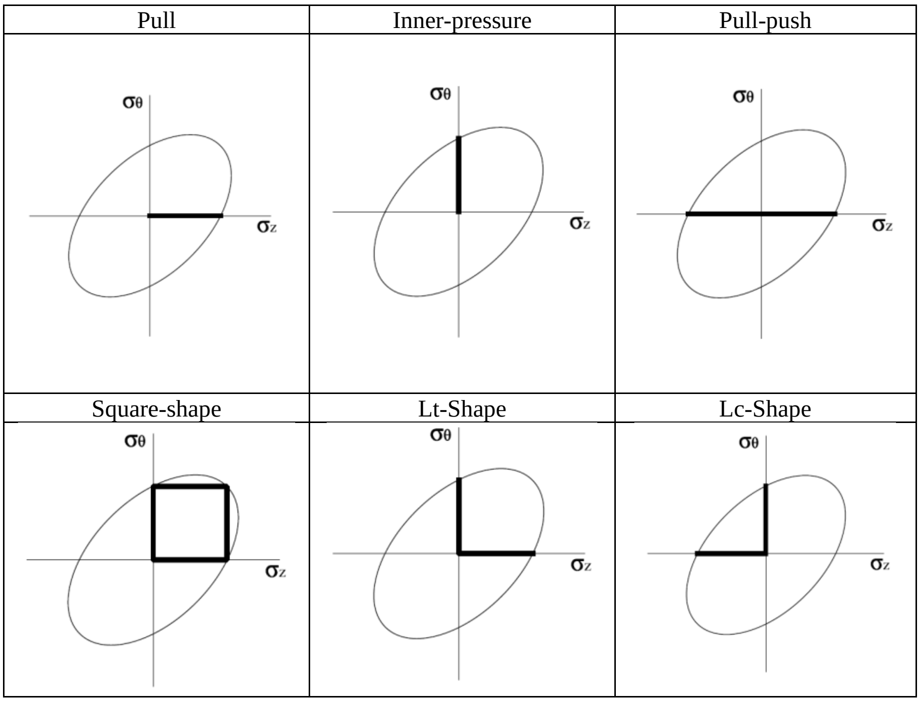
Pull

Inner-pressure

Pull-push

Square-shape

Lt-Shape

Lc-Shape

Figure 3. Schematic of the loading paths studied.

Fig. 4 and Fig. 5 show the von Mises equivalent strain amplitude, ε_{eqa}, and the von Mises mean strain, ε_{eqm}, respectively, for each test. It is observed that loading cases 3 and 4 fall within low cycle fatigue (LCF), cases 5, 6A and 6B fall in the medium cycle fatigue (MCF) regime and cases 1A and 1B are in the high cycle fatigue (HCF) regime [28]. ε_{eqm} presents a sigmoidal curve with a stable growth for all tests at middle life, that is, there is not a stabilised histeresys loop in any test and the material is constantly accumulating plastic strain. Fig. 4 shows that for most tests the strain amplitude initially decreases drastically, which is indicative of cyclic hardening. The initial drop is followed by a very slight increase up to ~2000 cycles in most tests. Beyond ~2000 cycles, the strain amplitude remains essentially constant, with the exception of tests 4 and 5. The drastic decrease in strain amplitude is caused by material cyclic hardening. The consequent gradual increase in the strain amplitude is caused by the cycle-dependent creep or ratcheting, whereby the plastic strain accumulates after each cycle. The ratcheting effect can be observed as increasingly mean strain Fig. 5, after the initial hardening. Similar bahaviour was also found previously on 316FR material [29]. The ratcheting analysis of uniaxial specimens subjected to different load ratios R under stress-control showed an increment of the strain range $\Delta\varepsilon$ in each cycle. Similar behaviour was also observed on 304 stainless steel subjected to different levels of uniaxial loads with the ratchetting strain, leaning towards a saturated state [30]. Higher levels of ratcheting were observed as the mean stress increased.

It is observed that for tests which include cyclic inner pressure (tests 2, 4, 5, 6A and 6B in Table 5), the fatigue life is improved as the ε_{eqa} increases. Test 4 shows an additional hardening after the first 10 cycles, with a reduction of the strain amplitude in each cycle up to ~2000 cycles. This behaviour is probably caused by additional slip planes activated [31]. Additional slip planes include the maximum shear strain range plane and the planes in the radial direction. Fig. 5 shows that the mean value increases during the entire life for all the tests. This means that no stabilised loop was achieved on any of the tests.

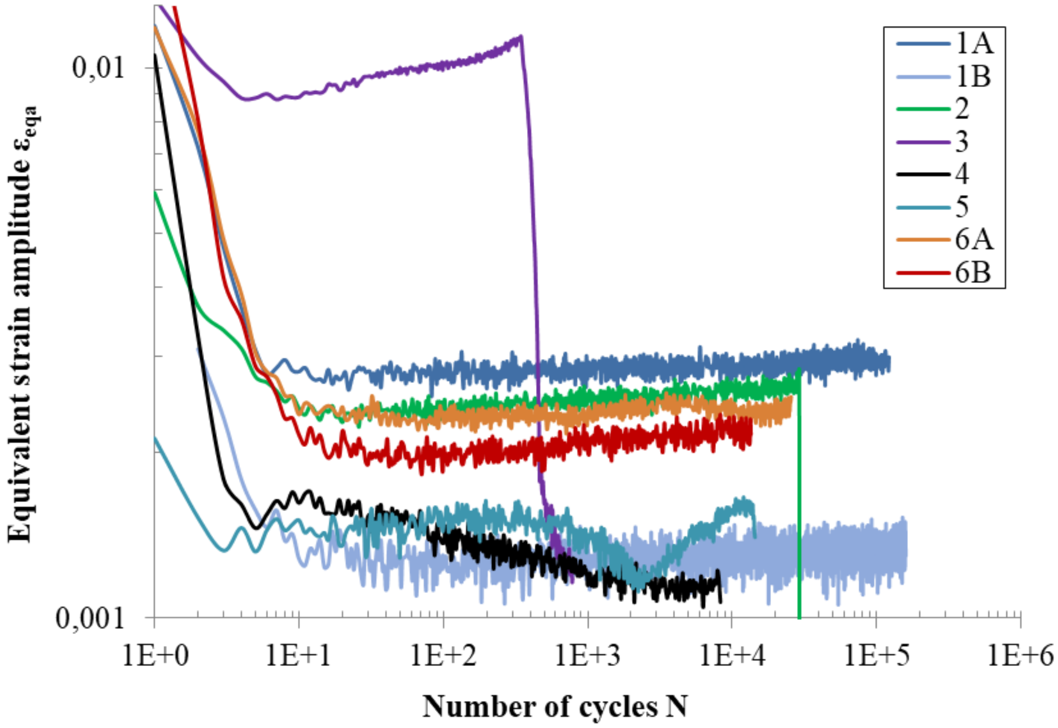

Figure 4. Equivalent von Mises strain amplitude. Variables are plotted against number of cycles, N, for each loading path.

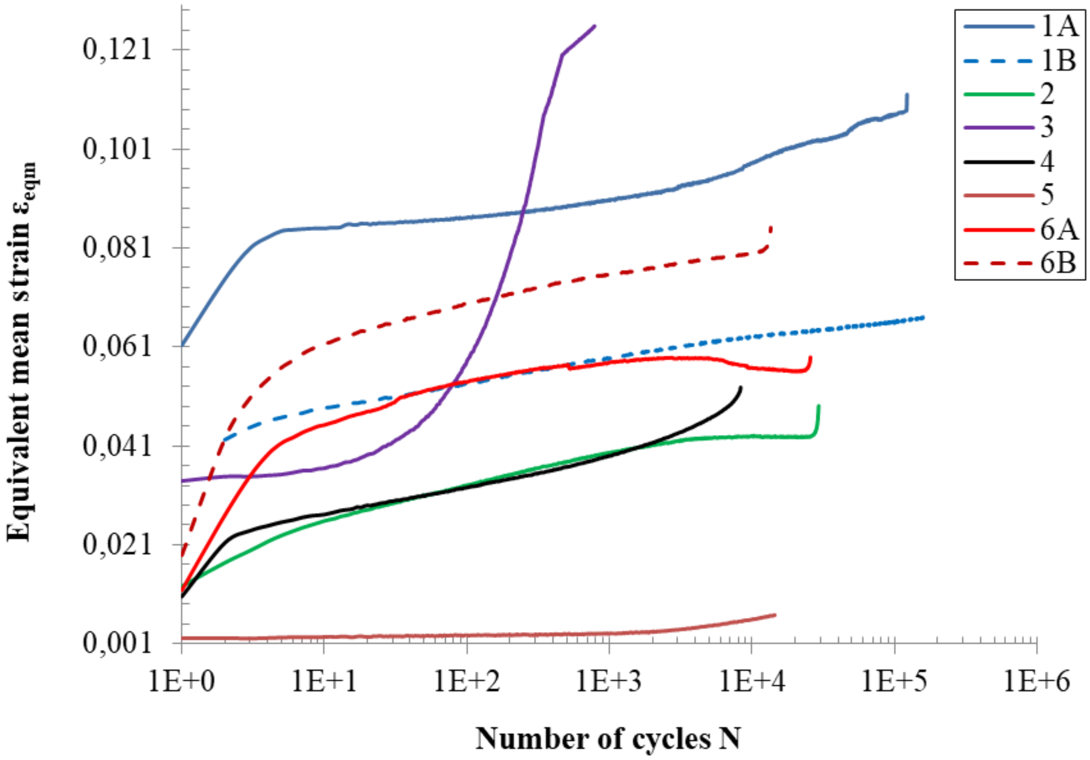

Figure 5. Equivalent von Mises mean strain. Variables are plotted against number of cycles, N, for each loading path.

The axial stress is calculated with Equation (1), the hoop and the radial stresses in the elastic region are calculated considering thick walled cylinders with Equations (2) and (3) [32], respectively.

$$\sigma_Z = \frac{F}{\pi(r_o^2 - r_i^2)} + \frac{Pr_i^2}{r_o^2 - r_i^2} \tag{1}$$

$$\sigma_\theta = \frac{Pr_i^2}{r_o^2 - r_i^2}\left[1 + \frac{r_o^2}{r^2}\right] \tag{2}$$

$$\sigma_R = \frac{Pr_i^2}{r_o^2 - r_i^2}\left[1 - \frac{r_o^2}{r^2}\right] \tag{3}$$

where F is the force applied, P the inner pressure introduced, r_o the outer radius, r_i the inner radius and r is the radius where the hoop and radial stresses are calculated. The stresses and strains on different planes φ are calculated considering the coordinate system and angles shown on Fig. 6. The normal vector n, perpendicular to the plane φ, is defined with the angle β between n and the axial load direction Z and the angle α between n and the radial direction R. Note that φ is not an angle, but rather the name of the critical plane predicted by each model. The orientation of φ plane is described in Fig. 6 by the angles α and β.

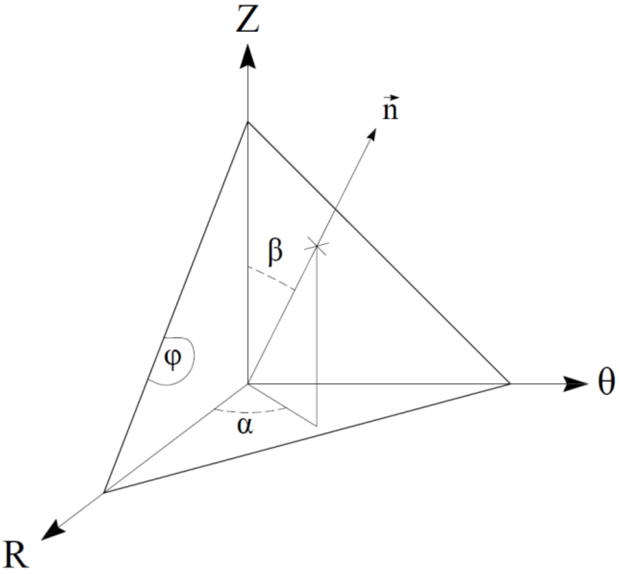

Figure 6. Definition of orientation of plane φ according to the three-dimensional coordinate system.

Due to the high level of mean hoop strain, the hoop stresses are corrected with the strain values observed at half-life fatigue so that the change in radius is taken into account. The corrected inner and outer diameter d^*_i and d^*_o are calculated following Equations (4) and (5), respectively.

$$d_o^* = d_o(1 + \varepsilon_{\theta m}) \tag{4}$$

$$d_i^* = \left[d_o^2((1 + \varepsilon_{\theta m})^2 - 1) + d_i^2\right]^{0.5} \tag{5}$$

where d_o is the initial outer diameter, d_i the initial inner diameter and $\varepsilon_{\theta m}$ the mean hoop strain at half-life fatigue.

Equation (2) indicates that the highest hoop stress appears at the inner surface of the specimen. The stress level decreases through the thickness so that the stress level at the outer surface is minimum. Nevertheless, most experimental techniques for measuring the strains provide information only from the external surface. Experimental systems such as strain gauge, extensometer, replica technique [33–35], digital image correlation [36], Moiré interferometry [37] or electronic speckle pattern interferometry [38] can be used for measuring the strain at certain spot or across an area. Information from the interior of the material can only be measured experimentally in most engineering materials via synchrotron X-ray diffraction [39,40], though access to such facilities is extremely limited (e.g. [41]). That is, even though Equations (2) and (3) indicate that strain levels at the outer surface are lower, fatigue predictions are normally made with those strains [16,31,42], thus being non conservative. In the next section we provide a numerical estimation of the residual stresses caused by the internal pressure. It will be shown that the residual stress profile tends to decrease the maximum stress at the inner surface and increase the stress at the outer surface once it yields, thereby reducing the difference between both surfaces and compensating the stresses on both sides of the wall.

4. RESIDUAL STRESS EVALAUTION

The residual stress generated by inner pressure applied was assessed numerically with a finite element model. The simulation was performed with ANSYS commercial software by applying inner pressure following a sinus function. Due to the symmetry of the specimen, one fourth of the cross section was simulated. Zero pressure was applied on the outer surface. The mesh was defined with 255 quadrilateral elements and 878 nodes. Plane strain theory was assumed since the strain in the Z direction approached zero (thick wall tubes). Chaboche's nonlinear kinematic hardening model was considered [43]. The material parameters used were obtained by fitting Equation (6) to 316 stainless steel cyclic experimental data available in the literature [11].

$$\frac{\Delta\sigma}{2} - K - R = \sum_{i=1}^{n} \frac{C_i}{\gamma_i} \tanh\left(\gamma_i \frac{\Delta\varepsilon^{pl}}{2}\right) \tag{6}$$

For each stabilised hysteresis loop, $\Delta\sigma/2$ is the stress amplitude, K is the initial yield stress, R is the isotropic variable; together define the yield zone size and the sum of both is obtained as half the elastic stress range, C_i is the hardening modulus, γ_i is the rate of decrease of hardening, $\Delta\varepsilon^{pl}/2$ is the plastic strain amplitude and n is the number of kinematic models to use. The fitted curve is shown in Fig. 7, with C_1=143670 γ_1=1200, C_2=12200, γ_2=0.22.

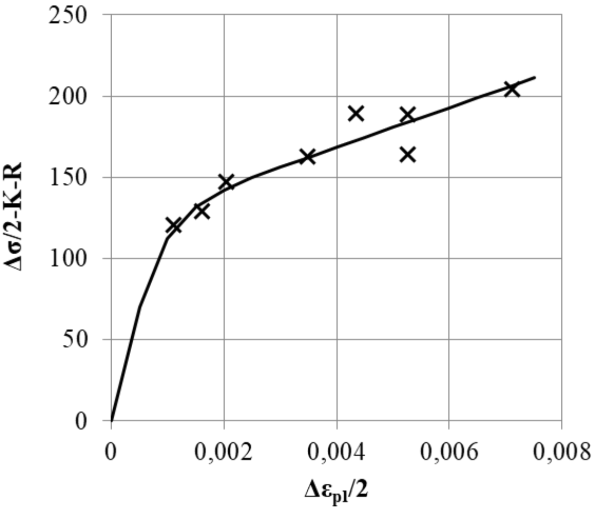

Figure 7. Fitted curve to cyclic experimental data of 316 stainless steel.

Fig. 8 shows the evolution of the hoop stress through two cycles at the inner and outer surfaces. When the inner surface yields (t~95s), the material reduces its stress accumulation capacity, thereby appears a redistribution of the stresses in order to maintain the equilibrium with the inner pressure. For the maximum load (t=180s), the generated stress is larger than the yield stress in all the thickness. Such plastic deformation of the specimen induces a volume mismatch that acts by inducing compressive residual stresses in the inner surface and tensile residual stresses at the outer surface. The resultant residual stress distribution in the hoop direction is shown in Fig. 9 for a 60 MPa inner pressure. An evolution from compressive stresses at the inner surface of the specimen to tensile stresses in the outer surface is observed.

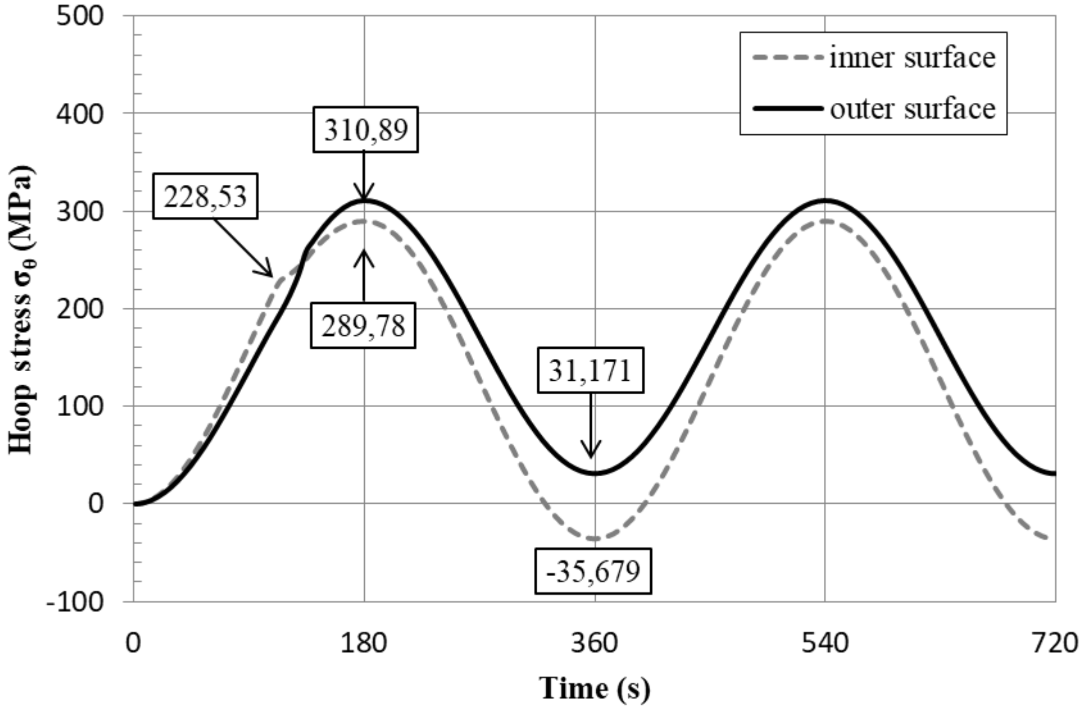

Figure 8. Evolution of the hoop stress along two cycles at the inner and outer surface applying 60 MPa inner pressure.

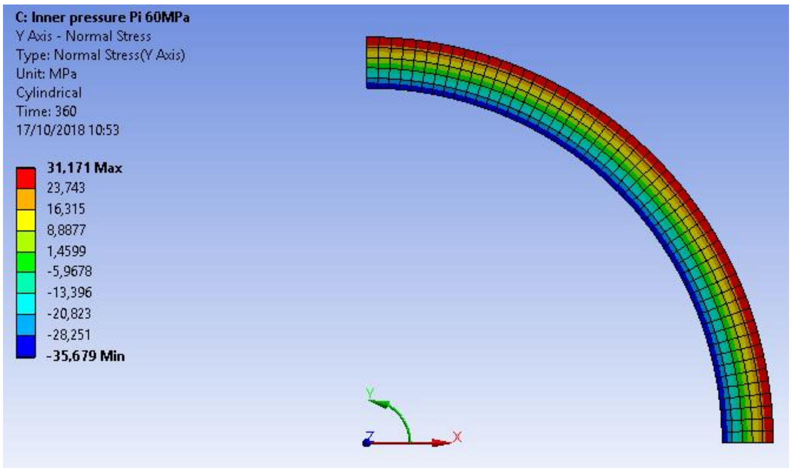

C: Inner pressure Pi 60MPa
Y Axis - Normal Stress
Type: Normal Stress(Y Axis)
Unit: MPa
Cylindrical
Time: 360
17/10/2018 10:53

Figure 9. Residual hoop stresses on inner and outer surface after applying 60 MPa inner pressure.

Fig. 10 shows the residual stress profile at the inner and outer surfaces once the pressure was removed. When the hoops stress generated by inner pressure exceeds the yield stress, different levels of plastic strain on the radial direction are generated, thus inducing residual stresses. After that, for lower levels of pressure, hoop stress will present an offset from the maximum values. This phenomenon is known as autofrettage and is a widely used manufacturing technique to enhance fatigue resistance of vessel and pipes under pressure. It is worth noting that one of the key issues for such industrial procedure is to evaluate the optimum autofrettage pressure to obtain an adequate residual stress at the inner surface [32,44,45]. Fig. 10 indicates that applying the largest inner pressure induces maximum values of residual stress, both in tension (on the outer surface) and compression (on the inner surface). Accordingly, subsequent cycles of hoop stress will be less damaging for the inner layers of the cylinder because inner layers are protected by compressive residual stress. Conversely, subsequent cycles of hoop stress will produce an additional damage on the outer layers of the cylinder because the applied stress will add to the tensile residual stress created by previous cycles. For the tests that include cyclic inner pressure loadings, Table 5, the hoop stress produces yielding through the entire thickness. This is called full autofrettage. The plane-strain stress distribution in this case can also be aproximated with the Equation (7) and (8) for the hoop and radial stress respectively [46].

$$\sigma'_\theta = \frac{2\sigma_{ys}}{\sqrt{3}}\left[1 + \ln\frac{r}{r_o} - \frac{r_i^2}{r_o^2 - r_i^2}\left(1 + \frac{r_o^2}{r^2}\right)\ln\frac{r_o}{r_i}\right] \tag{7}$$

$$\sigma'_R = \frac{2\sigma_{ys}}{\sqrt{3}}\left[\ln\frac{r}{r_o} - \frac{r_i^2}{r_o^2 - r_i^2}\left(1 - \frac{r_o^2}{r^2}\right)\ln\frac{r_o}{r_i}\right] \tag{8}$$

where σ_{ys} is the yield stress of the material r is the radius where the stress is calculated, r_o is the outer radius and r_i the inner radius. These residual stresses are considered to obtain the total stress values.

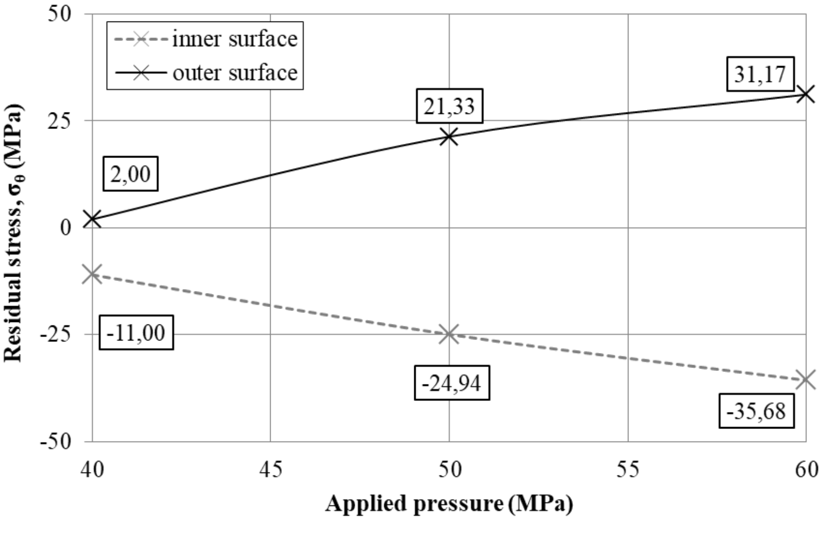

Figure 10. Residual stress created by different applied hoop pressures in the specimen. The residual stress is shown on the inner (dashed line) and outer (solid line) surfaces.

5. CRITICAL PLANE MODELS

The critical plane models used in this analysis were Fatemi-Socie (FS) [47], Wang-Brown (WB) [48] and Liu I and Liu II [9]. The FS and WB models are strain-based models and Liu I and Liu II are energy-based models. The four models include the total strain ranges in the damage parameter. As the strains are the principal factor on LCF regime, better results are will be expected on that regime. Among the different models considered, only Liu I determined directly the dominant tensile failure. FS and WB models consider the crack growth on the maximum shear strain plane (i.e. dominant shear failure) and both include a material parameter that controls the weight of the normal component (stress or strain) on the damage parameter. Liu II model is also defined for dominant shear failure.

Wang-Brown model (Equation 9) is a strain type model. The damage parameter is defined on the plane φ^* with the maximum shear strain range $\Delta\gamma$. The original equation is corrected to take into account the mean stress effect $\sigma_{n,mean}$, thus reducing the fatigue strength coefficient σ'_f. Both shear strain and normal strain in φ^* are considered in the Wang-Brown damage parameter. According to the authors, the physical explanation of such criterion is that cyclic shear strain promotes crack nucleation. At the same time, crack growth is a consequence of normal strain.

$$\frac{\Delta\gamma_{\max}}{2} + S\Delta\varepsilon_n = [(1+\nu_e) + S(1-\nu_e)]\frac{(\sigma'_f - 2\sigma_{n,mean})}{E}(2N_f)^b + [(1+\nu_p) + S(1-\nu_p)]\varepsilon'_f(2N_f)^c \qquad (9)$$

where $\Delta\gamma_{\max}/2$ is the maximum shear strain amplitude, $\Delta\varepsilon_n$ is the range of normal strain, υ_e and υ_p are the Poisson's ration in the elastic and plastic regimes, respectively, E is the Young modulus, σ'_f is the fatigue strength coefficient, b the fatigue strength exponent, ε'_f the fatigue ductility coefficient and c the fatigue ductility exponent, $\sigma_{n,mean}$ is the mean normal stress at half fatigue life. S parameter (Equation 10) defines the material sensitivity to the normal strain in the crack growth and can be estimated from the fatigue life, N_f.

$$S = \frac{\frac{\tau'_f}{G}(2N_f)^{b_\gamma} + \gamma'_f(2N_f)^{c_\gamma} - (1+\nu_e)\frac{\sigma'_f}{E}(2N_f)^b - (1+\nu_p)\varepsilon'_f(2N_f)^c}{(1-\nu_e)\frac{\sigma'_f}{E}(2N_f)^b + (1-\nu_p)\varepsilon'_f(2N_f)^c} \tag{10}$$

where G is the shear modulus and τ'_f the shear fatigue strength coefficient, b_γ the shear fatigue strength exponent, γ'_f the shear fatigue ductility coefficient and c_γ the shear fatigue ductility exponent.

Fatemi-Socie model (Equation 11) [47] is a strain type model, based upon the model proposed by Brown and Miller [15]. They suggested using normal stress component instead of the normal strain component, this allows including hardening and mean-stress effects into the model. The damage parameter is defined on the plane φ^* with the larger shear strain range $\Delta\gamma$. The normal stress on φ^* is modified by the coefficient k which defines the material sensitivity with respect the normal stress on the slip plane.

$$\frac{\Delta\gamma_{max}}{2}\left(1 + k\frac{\sigma_{n,max}}{\sigma_y}\right) = \frac{\tau'_f}{G}(2N_f)^{b_\gamma} + \gamma'_f(2N_f)^{c_\gamma} \tag{11}$$

where $\Delta\gamma_{max}/2$ is the maximum shear strain amplitude, $\sigma_{n,max}$ is the maximum axial stress at φ^*, σ_y is the yield stress, G is the shear modulus, τ'_f the shear fatigue strength coefficient, b_γ the shear fatigue strength exponent, γ'_f the shear fatigue ductility coefficient and c_γ the shear fatigue ductility exponent. k parameter can be estimated from the fatigue life, N_f (Equation 12). The mean stress is included in $\sigma_{n,max}$, so it is taken into account by the correction factor k.

$$k = \left[\frac{\frac{\tau'_f}{G}(2N_f)^{b_\gamma} + \gamma'_f(2N_f)^{c_\gamma}}{(1+\nu_e)\frac{\sigma'_f}{E}(2N_f)^b + (1+\nu_p)\varepsilon'_f(2N_f)^c} - 1\right]\frac{\sigma'_y}{\sigma'_f(2N_f)^b} \tag{12}$$

where υ_e and υ_p are the Poisson's ration in the elastic and plastic regimes, respectively, E is the Young modulus, σ'_f is the fatigue strength coefficient, b the fatigue strength exponent, ε'_f the fatigue ductility coefficient, c the fatigue ductility exponent and σ'_y is the cyclic yield stress.

Liu I (Equation 13 and 14) and Liu II (Equation 15 and 16) are energy type models [16]. Depending on the failure mode, Liu presents two parameters, one for a dominant normal tension failure, ΔW_I, and another one for a dominant shear tension failure, ΔW_{II}. Thus, the Liu models describe for a certain material and service condition, also the brittle or ductile behaviour of the material. For a dominant normal tension failure, the plane φ* will be the one that maximises the axial work ΔW_I (Equation 13). For a dominant shear tension failure, the plane φ* will be the one that maximises the shear work ΔW_{II} (Equation 15).

$$\Delta W_I = (\Delta\sigma_\mathrm{n}\Delta\varepsilon_\mathrm{n})_\mathrm{max} + (\Delta\tau\Delta\gamma) \tag{13}$$

where $\Delta\sigma_n$ is the normal stress range, $\Delta\varepsilon_n$ is the normal strain range, Δτ is the shear stress range and Δγ is the shear strain range.

$$\Delta W_I = 4\sigma'_\mathrm{f}\varepsilon'_\mathrm{f}(2\mathrm{N_f})^{\mathrm{b+c}} + \frac{4\sigma'^2_\mathrm{f}}{\mathrm{E}}(2\mathrm{N_f})^{\mathrm{2b}} \tag{14}$$

where σ'_f is the fatigue strength coefficient, b the fatigue strength exponent, ε'_f the fatigue ductility coefficient, c the fatigue ductility exponent and E is the young modulus.

$$\Delta W_{II} = (\Delta\sigma_\mathrm{n}\Delta\varepsilon_\mathrm{n}) + (\Delta\tau\Delta\gamma)_\mathrm{max} \tag{15}$$

where $\Delta\sigma_n$ is the normal stress range, $\Delta\varepsilon_n$ is the normal strain range, Δτ is the shear stress range and Δγ is the shear strain range.

$$\Delta W_{II} = 4\tau'_\mathrm{f}\gamma'_\mathrm{f}(2\mathrm{N_f})^{\mathrm{b}\gamma+\mathrm{c}\gamma} + \frac{4\tau'^2_\mathrm{f}}{\mathrm{G}}(2\mathrm{N_f})^{2\mathrm{b}\gamma} \tag{16}$$

where τ'_f the shear fatigue strength coefficient, b_γ the shear fatigue strength exponent γ'_f the shear fatigue ductility coefficient, c_γ the shear fatigue ductility exponent and G is the shear modulus.

5.1. Fatigue life predictions

The damage parameter of each model was obtained using half-life fatigue stress and strain values [42]. Fig. 11 shows fatigue life estimation for each model for different (a) uniaxial and (b) biaxial (outer surface) loading paths. The solid line presents those points with a coincidence between the experimental life N_{exp} and the calculated life N_{mod}. Dashed lines limit the zone with a twice (100%) and half (-50%) deviation of the calculated life respect to the experimental. The ID (Table 5) is also shown in Fig. 11 next to each predicted value. Fig. 12 shows the fatigue life deviation for each loading path.

Fig. 11 shows that in general the models tend to give conservative estimations for uniaxial tests (Fig. 11a) and non-conservative estimations for biaxial tests (Fig. 11b). All models produced high conservative fatigue life predictions for test 1A. Most of fatigue life predictions are found in the limiting zone of twice and half deviation. Since the critical plane models studied do not include mean strain parameters, ratchetting or mean strain effect appears to have a reduced effect on 316 stainless steel fatigue life. This is in agreement with a previous work from Kamaya [49], where the mean strain had a small influence on the fatigue life for constant strain ranges on the same material.

Liu I and Liu II models (equations 13 and 15) do not include any additional term to take into account mean stress effect. Liu assessed these models with the experimental data obtained by Zhang and Akid [50] for 316L with static tension and torsion. Liu observed a good correlation with fatigue life using Liu II model for tests with positive static stress, as the effect on the fatigue life observed was reduced. In this study, Liu II model returned good predictions with the studied loading path, with positive and negative mean stress. Mean stress effect appear to have little influence for the loading paths studied because Liu II model produces good predictions, even though it does not include any mean stress effect. The overall better estimations of Liu II as compared to Liu I indicate that 316 stainless steel failure mode is predominantly Mode II, on maximum shear strain plane. The large deviation given by Liu I for tests 4 and 5 is probably due to the way the critical plane is defined (maximum $\Delta\varepsilon\Delta\sigma$). The plane is parallel in both cases to one of the applied forces along the cycle. This way the plane defined is not affected by the second part of the loading path.

Fig. 11 shows that WB model estimations are the most conservative in general, both under uniaxial and biaxial loading. Mean stress correction on WB was done following Morrow's method [51]. Similar behaviour was previously observed on ST52-3N material subjected to 24 different proportional and non-proportional biaxial loads [10] and also with 1Cr-18Ni-9Ti stainless steel for non-proportional load[52]. In those cases, as suggested by Chen [50], using the maximum normal stress instead of the normal strain range allows the additional hardening to be taken into account more accurately. The mean stress effect with ratchetting appears to be low for the loading paths studied on the 316 stainless steel. WB damage parameter is based strain values measured on the outer surface, which are lower than on the inner surface. Accordingly, if the average strain values through the thickness were taken into account, the WB predictions would be even lower, thus producing more conservative predictions.

The only stress term in WB model is the mean stress term. Mean stress effect has little influence on the 316 stainless steel under study for the loading paths considered. For such cases, a new version of WB could be proposed that takes into account only the strains on the outer surface. Such version would be very appropriate for types of loading similar to these studied here and appear to be ideal for full-field experimental techniques such as Moiré interferometry[53], electronic speckle pattern interferometry [54] or digital image correlation [55] that measure a detailed displacement field across the surface [19].

Comparison between tests 2 and 6A is useful to understand the sensitivity of the material to the different types of load. Both test 2 and test 6A are subjected to the same inner pressure. However, test 6A is also subjected to compressive loads. Table 5 indicates that the fatigue life for test 6A is slightly smaller than for test 2. This suggests that the influence of compressive loads combined with inner pressure is little compared to different combinations of tensile loads [16].

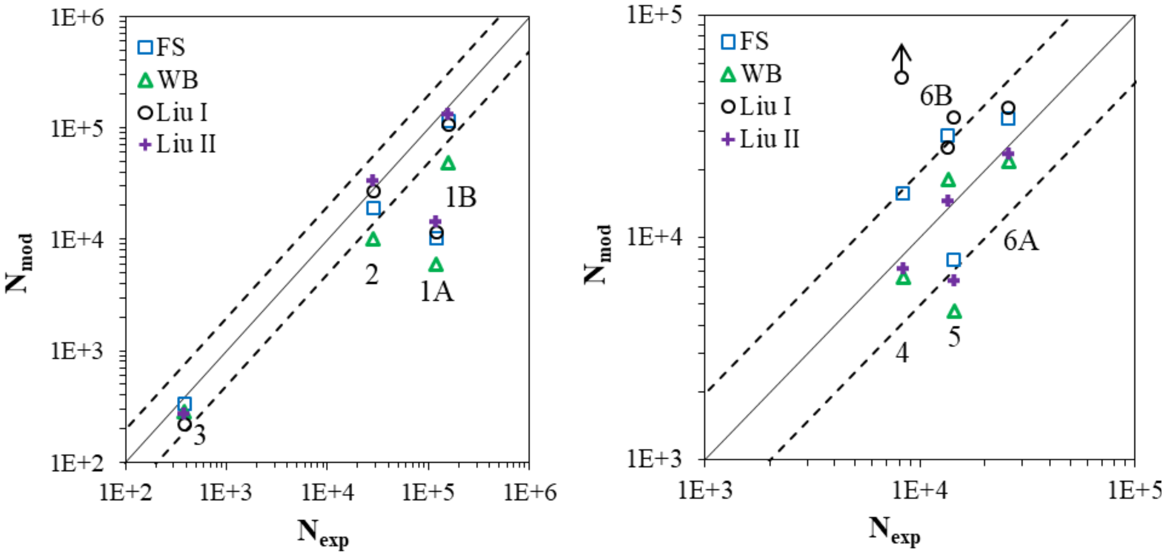

(a) (b)

Figure 11. Critical plane model fatigue life predictions for uniaxial (a) and biaxial (b) loading paths tests in 316 stainless steel.

The differences between the experimental and the calculated lives are summarised in Fig. 12. The differences are shown as a histogram of the life estimation deviation for each test according to the different models. The overall performance of each model can be estimated with the sum of the absolute deviations for all the tests and are as follows: FS - 4.45; WB - 3.96; Liu I - 16.34; and Liu II - 2.34. These values together with Fig. 11 indicate that Liu II appears to generate the best predictions overall. Moreover Liu II predictions are mostly on the conservative side. WB model appears to give the best predictions after Liu II model, followed by FS model and finally by Liu I model. This is in agreement with previous studies conducted by Liu on 316 stainless steel subjected to axial-torsion loading [9].

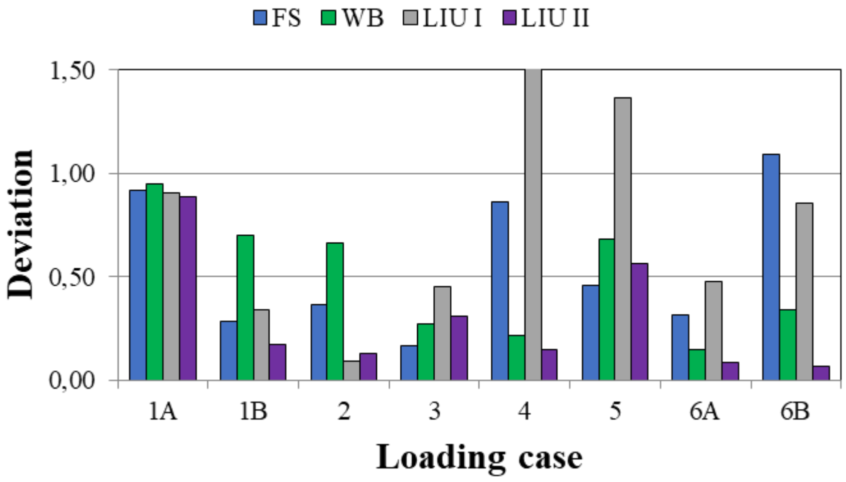

Figure 12. Model fatigue life deviation in each loading case

5.2. Crack orientation results

The cracking angle at initiation was measured with respect the longitudinal axis of the specimen (Fig. 13). Measurement of the angle was done with ImageJ open software [56] used for image processing. The cracking angles at initiation for the different tests are summarised in Table 5. The critical plane φ* is defined with the vector normal to the cracking plane, n, with the angles β and α between the longitudinal and radial axis respectively Fig. 6. The angle definition is shown in Fig. 13 for inner pressure test. The crack shown in Fig. 13 grows vertically (i.e. angle β = 90º). The angles measured on the surface were 0º or 90º in all cases, as shown in Table 5.

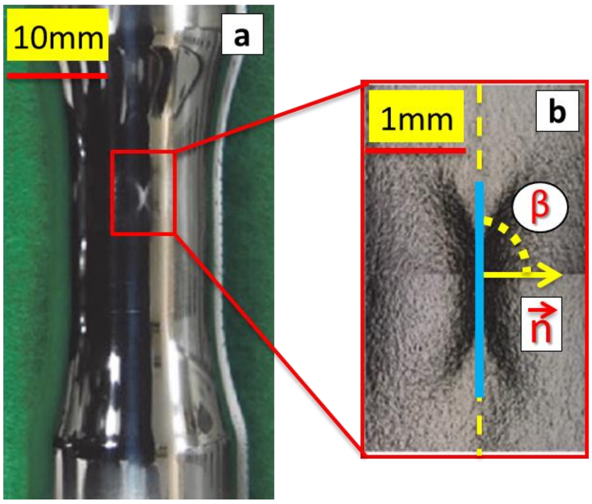

Figure 13. a) Picture of the central part of the specimen and b) schematic showing how the angle β and the normal vector, n, are defined for α angle 90º.

Table 5. Comparison of crack angles β and α at initiation measured with studied models predictions.

	ID	1A	1B	2	3	4	5	6A	6B
Angle measured	β / α	-/0º	-/0º	90º/-	-/0º	90º/-	90º/-	90º/-	90º/-
Wang-Brown	β / α	45º/0º	45º/0º	90º/45º	45º/0º	45º/90º	45º/90º	75º/45º	75º/45º
Fatemi-Socie	β / α	45º/0º	45º/0º	90º/45º	45º/0º	45º/90º	45º/90º	75º/45º	75º/45º
Liu I	β / α	0º/0º	0º/0º	90º/0º	0º/0º	0º/0º	90º/90º	90º/90º	90º/90º
Liu II	β / α	45º/0º	45º/0º	90º/45º	45º/0º	45º/90º	45º/90º	75º/45º	75º/45º

The cracking plane predicted by each model is compared to the critical plane predicted by the different models. Table 5 shows the predicted plane angle by the studied models. The critical plane φ* according to FS and WB is defined as the plane with maximum shear strain range, Liu II defines φ* at the plane where is maximised the shear work ΔW_{II}. On the other hand, Liu I defines φ* at the plane where the axial work ΔW_I is maximised. The crack orientation has also been studied previously by other researchers as the plane where the damage parameter is maximised [10], observing an offset with the critical plane φ* defined by each model. This criteria is recommended for non-proportional loadings, where critical plane could not be defined on the plane of maximum damage [6]. All the models appear to predict correctly the cracking angle for the uniaxial tests. For biaxial tests, Liu I shows better results than the other models. Nevertheless, previous works showed that FS and Liu II give better crack orientations with AISI 303 and 316 stainless steel under proportional and non-proportional loadings [9,21].

6. CONCLUSIONS

In this work, a characterisation of the fatigue behaviour of 316 stainless steel has been presented. The study includes uniaxial stress and multiaxial stress scenarios on the LCF, MCF and HCF regime with high levels of hardening and ratchetting. Unlike previous other works, this work analyses the effect of inner pressure based on four different critical plane models. To this end, a comparative study has been developed on the prediction capabilities of Wang-Brown, Fatemi-Socie, Liu I and Liu II models. Both fatigue life and cracking plane at initiation have been studied with the critical planes. Fatigue life estimations were calculated on the outer surface of the specimen. Overall good results were obtained for all loading paths. The sum of fatigue life deviations indicates that Liu II model provides the best predictions, followed by Wang-Brown, Fatemi-Socie and finally Liu I model. In addition, the predictions given by Liu II model felt in the conservative side. Previous analyses performed also showed better performance of Liu II model than Liu I model on the same material. Based on the good predictions of Liu II model, it appears that the mean stress effect has a small impact on the fatigue life for the loads studied. The small effect of the mean stress is confirmed with the good predictions obtained with FS with very small values of the k parameter that takes into account the mean stress effect. Moreover, this fact is confirmed by the good agreement with previous works that employed FS and WB models without mean stress effect [19]. The failure plane was also assessed with the critical plane models. The best failure plane predictions were obtained with Liu I model. The three other models (Wang-Brown, Fatemi-Socie and Liu II) predicted the same cracking angle because they are all based on the same critical plane. The current work also suggests that the ratchetting effect has little influence on the prediction of the fatigue life on 316 stainless steel.

ACKNOWLEDGEMENTS

Financial support from Ministerio de Economia y Competitividad through grant reference MAT2016-76951-C2-2-P is greatly acknowledged.

REFERENCES

1 Papuga J, Vargas M, Hronek M. Evaluation Of Uniaxial Fatigue Criteria Applied To Multiaxially Loaded Unnotched Samples. *Engineering Mechanics*. 2012;19: 99–111.

2 Chu C-C. Multiaxial fatigue life prediction method in the ground vehicle industry. *International Journal of Fatigue*. 1997;19: S325–S330.

3 Wang YY, Yao WX. Evaluation and comparison of several multiaxial fatigue criteria. *International Journal of Fatigue*. 2004;26: 17–25.

4 Chen X, Gao Q, Sun XF. Damage analysis of low-cycle fatigue under non-proportional loading. *International Journal of Fatigue*. 1994;16: 221–225.

5 Lopez-Crespo P, Pommier S. Numerical analysis of crack tip plasticity and history effects under mixed mode conditions. *Journal of Solid Mechanics and Materials Engineering*. 2008;2: 1567–1576.

6 Socie DF, Marquis GB. *Multiaxial Fatigue*. Warrendale, PA (USA): Society of Automotive Engineers, Inc.; 2000.

7 Karolczuk A, Macha E. A review of critical plane orientations in multiaxial fatigue failure criteria of metallic materials. *International Journal of Fracture*. 2005;134: 267–304.

8 Erickson M, Kallmeyer AR, Van Stone RH, Kurath P. Development of a Multiaxial Fatigue Damage Model for High Strength Alloys Using a Critical Plane Methodology. *Journal of Engineering Materials and Technology*. 2008;130: 041008.

9 Liu K. A method based on virtual strain energy parameters for multiaxial fatigue life

prediction. *Advances in multiaxial fatigue, ASTM*. 1993: 67–84.

10 Lopez-Crespo P, Moreno B, Lopez-Moreno A, Zapatero J. Study of crack orientation and fatigue life prediction in biaxial fatigue with critical plane models. *Engineering Fracture Mechanics*. 2015;136: 115–130.

11 Chou LH, Chiou YC, Wu CC, Huang YJ. Predictions of stress-strain curve and fatigue life for AISI 316 stainless steel in cyclic straining. *Journal of Marine Science and Technology (Taiwan)*. 2016;24: 426–433.

12 Turski M, Bouchard PJ, Steuwer A, Withers PJ. Residual stress driven creep cracking in AISI Type 316 stainless steel. *Acta Materialia*. 2008;56: 3598–3612.

13 Tanaka K, Takahash H, Akiniwa Y. Fatigue crack propagation from a hole in tubular specimens under axial and torsional loading. *International Journal of Fatigue*. 2006;28: 324–334.

14 Chandra SK, Shankar V, Mariappan K, Sandhya R, Chakraborty PC. Effect of strain rate on the low cycle fatigue behavior of 316L(N) stainless steel weld joints. *Procedia Engineering*. 2013;55: 176–180.

15 Isobe K, Ohte S. Fatigue and Creep-Fatigue Testing of Bellows at Elevated Temperature. 2016;110.

16 Majumdar S. *Biaxial Creep-Fatigue Behavior of Type 316H Stainless Steel Tube*. Illinois; 1979.

17 Morishita T, Itoh T, Bao Z. Multiaxial fatigue strength of type 316 stainless steel under push-pull, Reversed torsion, Cyclic inner and outer pressure loading. *International Journal of Pressure Vessels and Piping*. 2016;139-140: 228–236.

18 Holmström S, Pohja R, Nurmela A, Moilanen P, Auerkari P. Creep and creep-fatigue behaviour of 316 stainless steel. *Procedia Engineering*. 2013;55: 160–164.

19 Jin D, Tian DJ, Li JH, Sakane M. Low-cycle fatigue of 316L stainless steel under proportional and nonproportional loadings. *Fatigue and Fracture of Engineering Materials and Structures*. 2016;39: 850–858.

20 Han C, Chen X, Kim KS. Evaluation of multiaxial fatigue criteria under irregular loading. *International Journal of Fatigue*. 2002;24: 913–922.

21 Reis L, Li B, de-Freitas M. Crack initiation and growth path under multiaxial fatigue loading in structural steels. *International Journal of Fatigue*. 2009;31: 1660–1668.

22 Del Llano-Vizcaya L, Rubio-Gonzalez C, Mesmacque G, Cervantes-Hernández T. Multiaxial fatigue and failure analysis of helical compression springs. *Engineering Failure Analysis*. 2006;13: 1303–1313.

23 Liu J, Kang JX, Yan WZ, Wang FS, Yue ZF. Prediction of fatigue performance of fastener holes with bolt clamping force based on critical plane approach. *Materials Science & Engineering A*. 2010;527: 3510–3514.

24 ASTM E2207 Standard Practice for Strain-Controlled Axial-Torsional Fatigue Testing with Thin-Walled Tubular Specimens. 2015.

25 Susmel L, Petrone N. Multiaxial fatigue life estimations for 6082-T6 cylindrical specimens under in-phase and out-of-phase biaxial loadings. In: Carpinteri A, M DF, Spagnoli A, eds. *Biaxial and Multiaxial Fatigue and Fracture, ESIS*. ; 2003:83–104.

26 Shang DG, Sun GQ, Deng J, Yan CL. Multiaxial fatigue damage parameter and life

prediction for medium-carbon steel based on the critical plane approach. *International Journal of Fatigue*. 2007;29: 2200–2207.

27 Chen X, Xu S, Huang D. Critical plane-strain energy density criterion for multiaxial low-cycle fatigue life under non-proportional loading. *Fatigue and Fracture of Engineering Materials and Structures*. 1999;22: 679–686.

28 Suresh S. *Fatigue of Materials*. Cambridge: Cambridge University Press; 2004.

29 Mizuno M. Uniaxial ratchetting of 316FR steel at room temperature—Part I: experiments. *Journal of …*. 2000;122: 29–34.

30 Kang G. Experimental study on uniaxial and nonproportionally multiaxial ratcheting of SS304 stainless steel at room and high temperatures. *Nuclear Engineering and Design*. 2002;216: 13–26.

31 Ellyin F, Gołoś K, Xia Z. In phase and out-of-phase multiaxial fatigue. *Transactions of the ASME*. 1991;113: 112–118.

32 Malik MA, Khushnood S. a Review of Swage – Autofrettage Process. *Conference on Nuclear Engineering*. 2003: 1–12.

33 Window AL. *Strain Gauge Technology*. (Springer Netherlands, ed.).1992.

34 Gomez C, Canales M, Calvo S, Rivera R, Valdes JR, Nunez JL. High and low cycle fatigue life estimation of welding steel under constant amplitude loading: Analysis of different multiaxial damage models and in-phase and out-of-phase loading effects. *International Journal of Fatigue*. 2011;33: 578–587.

35 Scherrer SS, Quinn JB, Quinn GD, Wiskott HWA. Fractographic ceramic failure analysis using the replica technique. *Dental Materials*. 2007;23: 1397–1404.

36 Mokhtarishirazabad M, Lopez-Crespo P, Moreno B, Lopez-Moreno A, Zanganeh M. Evaluation of crack-tip fields from DIC data: a parametric study. *International Journal of Fatigue*. 2016;89: 11–19.

37 Nicoletto G. Moiré interferometry determination of residual stresses in the presence of gradients. *Experimental Mechanics*. 1991;31: 252–256.

38 Shterenlikht A, Díaz-Garrido FA, Lopez-Crespo P, Withers PJ, Patterson EA. Mixed Mode (KI + KII) Stress Intensity Factor Measurement by Electronic Speckle Pattern Interferometry and Image Correlation. *Applied Mechanics and Materials*. 2004;1-2: 107–112.

39 Lopez-Crespo P, Steuwer A, Buslaps T, et al. Measuring overload effects during fatigue crack growth in bainitic steel by synchrotron X-ray diffraction. *International Journal of Fatigue*. 2015;71: 11–16.

40 Steuwer A, Santisteban J, Turski M, Withers PJ, Buslaps T. High-resolution strain mapping in bulk samples using full-profile analysis of energy dispersive synchrotron X-ray diffraction data. *Nucl Instr Meth Physics Research B*. 2005;238: 200–204.

41 http://www.esrf.eu/ Accessed 2 May 2018.

42 Fatemi A, Kurath P. Multiaxial fatigue life predictions under the influence of mean-stresses. *Journal of Engineering Materials and Technology*. 1988;110: 380–388.

43 Chaboche JL. Time-independent constitutive theories for cyclic plasticity. *International Journal of Plasticity*. 1986;2: 149–188.

44 Harvey J. *Theory and Design of Pressure Vessels*.1985.

45 Ayob A, Elbasheer MK. Optimum autofrettage pressure in thick cylinders. *Jurnal Mekanikal*. 2007: 1–14.

46 Hills R. *The Mathematical Theory of Plasticity*. Oxford University Press; 1950.

47 Fatemi A, Socie DF. A Critical Plane approach to multiaxial fatigue damage including out-of-phase loading. *Fatigue and Fracture of Engineering Materials and Structures*. 1988;11: 149–165.

48 Wang CH, Brown MW. A path-independent parameter for fatigue under proportional and non-proportional loading. *Fatigue & Fracture of Engineering Materials & Structures*. 1993;16: 1285–1298.

49 Kamaya M. Influence of mean strain on fatigue of stainless steel (effect of constant and ratchetting mean strain). In: *ASME 2014 Pressure Vessels and Piping Conference*. ; 2014:1–8.

50 Zhang W, Akid R. Mechanisms and fatigue performance of two steels in cyclic torsion with axial static tension/compression. *Fatigue and Fracture of Engineering Materials and Structures*. 1997;20: 547–557.

51 Socie DF, Morrow J. *Review of Contemporary Approaches to Fatigue Damage Analysis*. Illinois; 1976.

52 Chen X, An K, Kim KS. Low-cycle fatigue of 1Cr-18Ni-9Ti stainless steel and related weld metal under axial, torsional and 90 out-of-phase loading. *Fatigue and Fracture of Engineering Materials and Structures*. 2004;27: 439–448.

53 Nicoletto G. Experimental crack tip displacement analysis under smallscale yielding conditions. *International Journal of Fatigue*. 1986;8: 83–89.

54 Vasco-Olmo JM, Díaz FA, Patterson EA. Experimental evaluation of shielding effect on growing fatigue cracks under overloads using ESPI. *International Journal of Fatigue*. 2016;83(2): 117–126.

55 Mokhtarishirazabad M, Lopez-Crespo P, Zanganeh M. Stress intensity factor monitoring under cyclic loading by digital image correlation. *Fatigue and Fracture of Engineering Materials and Structures*. 2018;41: 2162–2171.

56 https://imagej.net/Welcome accessed November 2018.